



AMERICAN METEOROLOGICAL SOCIETY

Monthly Weather Review

EARLY ONLINE RELEASE

This is a preliminary PDF of the author-produced manuscript that has been peer-reviewed and accepted for publication. Since it is being posted so soon after acceptance, it has not yet been copyedited, formatted, or processed by AMS Publications. This preliminary version of the manuscript may be downloaded, distributed, and cited, but please be aware that there will be visual differences and possibly some content differences between this version and the final published version.

The DOI for this manuscript is doi: 10.1175/MWR-D-17-0194.1

The final published version of this manuscript will replace the preliminary version at the above DOI once it is available.

If you would like to cite this EOR in a separate work, please use the following full citation:

Müller, M., Y. Bartrak, J. Kristiansen, M. Køltzow, G. Noer, and A. Korosov, 2017: Characteristics of a convective-scale weather forecasting system for the European Arctic. *Mon. Wea. Rev.* doi:10.1175/MWR-D-17-0194.1, in press.



Characteristics of a convective-scale weather forecasting system for the European Arctic

Malte Müller*, Yurii Batrak, Jørn Kristiansen, Morten A. Ø. Køltzow, Gunnar Noer

Norwegian Meteorological Institute, Oslo, Norway

Anton Korosov

Nansen Environmental and Remote Sensing Center, Bergen, Norway

⁷ *Corresponding author address: Malte Müller, Development Center for Weather Forecasting , Norwegian Meteorological Institute, Oslo, Norway
⁸ E-mail: maltem@met.no

ABSTRACT

10 In this study we are comparing a one year data set of a convective-scale at-
11 mospheric prediction system of the European Arctic (AROME Arctic) with
12 the ECMWF's medium range forecasting, ensemble forecasting and reanaly-
13 sis systems, by using surface and radiosonde observations of wind and tem-
14 perature. The focus is on the characteristics of the model systems in the very
15 short-term forecast range (6 to 15 hours), but without a specific focus on lead
16 time dependencies. In general, AROME-Arctic adds value to the represen-
17 tation of surface characteristics. The atmospheric boundary layer thickness,
18 during stable conditions, is overestimated in the global models, presumably
19 due to a too diffusive turbulence scheme. Instead, AROME Arctic shows a
20 realistic mean thickness compared to the radiosonde observations. All mod-
21 els behave similarly for the upper air verification and surprisingly, as well, in
22 forecasting the location of a polar low in the short-range forecasts. However,
23 when comparing with the largest wind speeds from ocean surface winds and
24 at coastal synoptic weather station during land fall of a polar low, AROME
25 Arctic shows most realistic values. In addition to the model intercomparison,
26 we discuss in detail the limitation of the representation of sea-ice and ocean
27 surface characteristics on kilometer scales. This major challenge is illustrated
28 by showing the rapid drift and development of sea-ice leads during a cold air
29 outbreak. As well, the available sea surface temperature products and a high-
30 resolution ocean model result are compared qualitatively. New developments
31 of satellite products, ocean - sea-ice prediction models, or parameterizations,
32 tailored towards high-resolution atmospheric Arctic prediction, are necessary
33 to overcome this limitation.

³⁴ **1. Introduction**

³⁵ Over the past decades the Arctic warmed more than any other region in the world with profound
³⁶ socio-economic consequences. As a result, there is a growing demand for accurate Arctic weather
³⁷ predictions, which puts great expectation on our current global and regional forecasting systems
³⁸ (Emmerson and Lahn 2012; Jung et al. 2016). There are many challenges for Arctic weather
³⁹ prediction, e.g. the sparse observation network, atmospheric data assimilation, the representation
⁴⁰ of sea-ice, and the high-latitude representation of many sub-grid scale parameterizations (WMO-
⁴¹ PPP 2013; Vihma et al. 2014).

⁴²

⁴³ Global weather forecasting systems have a horizontal resolution of around 10 km and will in
⁴⁴ the near-future approach convective permitting scales, by reducing the grid spacing below \sim 4 km.
⁴⁵ Recent studies, based on global or pan-Arctic systems, showed that significant progress has
⁴⁶ been made in the last decades in improving forecasting skill, representation of uncertainties, and
⁴⁷ forecast analyses in the Arctic region (Jung and Leutbecher 2007; Jung and Matsueda 2016; Bauer
⁴⁸ et al. 2016; Bromwich et al. 2016; Hines and Bromwich 2017). Furthermore, as for example
⁴⁹ shown for the polar low representation in global analysis (Zappa et al. 2014), global systems are
⁵⁰ already able to resolve to some extent meso-scale high-latitude dynamics.

⁵¹

⁵² Regional model systems already have kilometer-scale resolution and thus, start to resolve con-
⁵³ vective atmospheric processes (e.g. Seity et al. 2010). Recent studies showed the use and advances
⁵⁴ of high-resolution regional versus coarser-resolution global model systems (Gutjahr et al. 2016;
⁵⁵ Moore et al. 2016; Smirnova and Golubkin 2017). However, to our knowledge, there has been no
⁵⁶ detailed study on analysing the characteristics of a convection permitting high-resolution system

57 for the Arctic regions. In the European Arctic the convective-scale weather prediction system
58 AROME Arctic is in operation since November 2015. Forecast analyses are derived by a 3DVAR
59 data assimilation scheme and observations from various sources, including synoptic, radiosonde,
60 airplane, and satellite data. It is the main Arctic weather forecasting tool used by the Norwegian
61 Meteorological Institute which has national and international responsibilities for weather, sea-ice,
62 and ocean prediction in large parts of the European Arctic. The recent entry-into-service of the
63 operational AROME Arctic is dedicated to improve the representation of physical phenomena,
64 to tackle challenges related to the observation (in-situ and remote sensing) network and to the
65 associated data assimilation methodologies, which all present unique challenges for polar regional
66 weather prediction. Data assimilation will be the subject of another study (Randriamampianina
67 pers. comm.). AROME Arctic is one of the core models of the Year Of Polar Prediction (YOPP)
68 and further, the AROME model system will be central for the coming high-resolution Arctic
69 reanalysis, as part of the Copernicus Climate Change Service.

70

71 The purpose of the present study is to extend previous studies on Arctic weather prediction by
72 comparing a convective-scale system with coarser-resolution model systems from the European
73 Center for Medium-range Weather Forecasts (ECMWF) Integrated Forecast System (IFS). We
74 are analysing a one-year record of very short-range forecasts (6 to 15 h) in order to assess the
75 model's ability to resolve characteristics of temperature and wind at the surface, boundary layer,
76 and in the upper troposphere and lower stratosphere. Moreover, the short-range predictability and
77 representation of a polar low is assessed. With near-surface wind speeds in excess of 15 m/s, polar
78 lows are the most intense systems in the family of polar mesoscale cyclones. These storms are
79 smaller and more transient than the more familiar and predictable synoptic-scale weather systems.
80 Residing poleward of the main polar front, polar lows can potentially be a hazard to high-latitude

81 marine operations, e.g. shipping, gas and oil platforms, and also affect land transport and aviation.

82

83 The paper is organized as follows. In Section 2 we give a brief description of the model systems.

84 The evaluation against surface and radiosonde observations is given in Section 3. In Section 4 a
85 detailed study of a polar low event is provided and in Section 5 we describe the current challenges
86 in the representation of sea-ice and ocean characteristics in the high-resolution model system. A
87 summary and a conclusion is provided in Section 6.

88 **2. Models**

89 A regional model, the convective-scale regional European Arctic forecasting system (AROME
90 Arctic) and three configurations of ECMWF global model system, the deterministic (HRES),
91 ensemble (ENS), and reanalysis (ERA Interim) (Bauer et al. 2013; Dee et al. 2011), are used in
92 the present study.

93

94 AROME Arctic is a regional high-resolution forecasting system for the European Arctic with
95 a horizontal resolution of 2.5 km and 65 vertical levels (Figure 1 and 2). The model is primarily
96 based on the HARMONIE AROME configuration (version 38h1.2) of the ALADIN-HIRLAM
97 numerical weather prediction system (Bengtsson et al. 2017). More details on the model system
98 are given in Seity et al. (2010) and on the Nordic set-up (AROME MetCoOp) in Müller et al.
99 (2017). AROME Arctic is currently very similar to the AROME MetCoOp setup and a large set
100 of conventional and satellite observations are assimilated by a 3DVAR and optimal interpolation
101 data assimilation systems, for upper air and and surface observations, respectively. The AROME
102 Arctic model is forced by HRES at the lateral and upper boundaries. The coupling zone in which

103 the AROME Arctic model is relaxed toward the large-scale coupling model is eight grid points
104 wide in the horizontal and the eight top-levels in the vertical (Davies 1976).

105 Because of the delayed availability of HRES forecasts, the analysis times of the HRES forecasts,
106 which are used as boundaries, are 6 h earlier than the actual forecast. The sea surface temperature
107 (SST) is re-gridded from the HRES, which, in turn, is based on the Operational sea Surface
108 Temperature and sea Ice Analysis (OSTIA, Donlon et al. 2012) from UK Met Office. Sea-ice
109 concentrations are obtained from the Ocean and Sea Ice Satellite Application Facilities (OSI-SAF,
110 Rasmus et al. 2016). The surface temperature over sea-ice is taken once from HRES (cold-start),
111 and is subsequently modelled by a 1D sea-ice model (Batrak et al. 2017).

112
113 A detailed description of the ECMWF model systems can be found in Bauer et al. (2013)
114 and Dee et al. (2011). ERA Interim is a fixed model system with a model resolution of around
115 80 km and 60 vertical levels (Figure 2). HRES and ENS model systems are under constant
116 development and a major change within our analysis period occurred 8 March 2016, where the
117 linear reduced Gaussian grid was changed to a cubic reduced Gaussian grid. With this change
118 the spectral truncation is unchanged but the grid-point space resolution is increased to more
119 accurately represent the physical processes and advection. Thus, in HRES and ENS the horizontal
120 resolution changed from 18 to 9 km and 36 to 18 km, respectively. The number of vertical levels
121 is 137 in HRES and 91 in ENS (Figure 2). A second change occurred 22 November 2016 (from
122 version 41r2 to 43r1), with main modifications in the ocean component ¹. Note, from ENS we are
123 using the control run only.

124

¹<http://www.ecmwf.int/en/forecasts/documentation-and-support/changes-ecmwf-model>

125 **3. Statistical Verification**

126 A statistical verification over a one-year period (1 December 2015 till 30 November 2016) is
127 performed. The focus of this study is on verification of temperature and wind only. The charac-
128 teristics of temperature and wind vary considerably from season to season (Figure 3). In between
129 October and May the variability of temperature and wind is high. Surface observations for
130 example at Bjørnøya, an island between the Norwegian mainland and the Svalbard Archipelago,
131 show abrupt temperature changes of up to 10 K and wind maxima of around 20 m/s. Instead, in
132 months, between May and September this variability is significantly smaller.

133

134 The larger atmospheric variability during the winter months is mainly caused by the large north-
135 south temperature gradient in winter and the alternation of northerly and southerly winds. In this
136 regard, an important winter pheonomenon are cold-air outbreaks (CAO). During CAOs cold air
137 masses are transported from ice-covered areas towards lower latitudes and sea-ice free areas. For
138 illustration we compute the CAO index from 6 h forecast of the AROME Arctic model (Figure
139 3). The index is defined by the difference of the 850 hPa potential temperature and surface skin
140 temperature (Papritz et al. 2015), and integrated over the area west of the Svalbard Archipelago.
141 This area is indicated in Figure 1 by a green box. The observed temperature and wind timeseries,
142 shown in Figure 3, are from the Bjørnøya observation site, which is located in the south-eastern
143 corner of the CAO index region (Figure 1). By comparing the major CAO events in the timeseries
144 with the wind and temperature observations, it shows, that the most abrupt temperature changes
145 and strongest winds are coinciding with larger CAO index values. Similar correlations can be
146 found for other observation timeseries in the European Arctic.

147 *a. Surface*

148 A set of 89 synoptic observations (Figure 1) and continuous timeseries of model forecasts,
149 which are initialized at 0000 UTC and 1200 UTC and have lead times of 6, 9, 12, and 15 h, are
150 used for verification. The observations are 3-hourly 2-meter temperature (T2M) and 10-meter
151 wind speed (U10M) from the Norwegian synoptic station network. For the verification of T2M,
152 a height correction (0.65 K per 100 m altitude) is applied to account for the different model
153 resolution and respective heights of the model's topography. The averaged (over all stations) root
154 mean square error (rmse) is shown for the verification period with a running mean filter (20-day
155 window) (Figure 4). Since the rmse also depends on the variability of signal in observation and
156 models, we computed the standard deviation from all records and it shows that the standard
157 deviation is 7.7 K for the observations and in between 7.4 and 7.6 k for the model systems. The
158 rmse of all models is larger during the winter months (October to May), for both T2M and U10M,
159 which is expected from the seasonal changes of the wind and temperature variability (Figure 3).
160 A sharp transition in the wind rmse, from about 3 to 2 m/s, is visible in the end of April for all
161 model systems. This transition can not originate from the model system updates in March 2016,
162 since the transition also exists for ERA Interim which has not been modified since its entry into
163 service.

164

165 For the rmse of the T2M there is a clear separation of the AROME Arctic model from the other
166 model systems. The differences are largest in winter and about 1 K. HRES shows consistently
167 lower rmse values than ENS and ERA Interim throughout the year. After the model updates
168 in March 2016, the rmse of ENS are smaller than those of ERA-Interim, however, differences

169 between those two model systems are small.

170

171 In a spatial comparison of the T2M rmse and bias, in between the AROME Arctic and HRES
172 model, we further divide into observed T2M below and above -10°C (Figures 5 and 6). The
173 division into these two temperature ranges follows the analysis of Atlaskin and Vihma (2012),
174 who found that in Nordic regions HRES and AROME have the largest positive bias during cold
175 conditions ($\text{T2M} < -10^{\circ}\text{C}$), which is often caused by temperature inversion and is underestimated
176 in the models. Indeed, largest positive model bias is found in cold conditions. Especially, at the
177 weather stations located further inland, HRES shows strong positive model bias (larger than 4 K).
178 For stations closer to the coast, the bias of HRES is predominantly negative. In AROME Arctic
179 T2M bias is about 1-2 K for T2M larger than -10°C and it varies between -2 and +2 K for T2M
180 below -10°C . In the Northern areas (Bjørnøya and Svalbard Archipelago), the forecast skill of the
181 models is similar. The reason for this could be attributed to issues of the representation of ocean
182 and sea-ice surface properties (see also Section 5), which cancel out the benefits gained from the
183 higher resolution.

184

185 The rmse for T2M lower than -10°C are very similar between AROME Arctic and HRES, with
186 values of 5 K in the inland and 2-4 K closer to the coast. For T2M larger than -10°C , HRES
187 shows largest RMSE values closer to the coast with values of up to 4 K, while AROME Arctic
188 has RMSE values predominantly of around 2-3 K.

189

190 The standard deviation of U10M is 3.5 m/s for the observations and 3.3 m/s for AROME Arctic.
191 The ECMWF model systems show significantly lower standard deviations with values between 2.7
192 and 2.8 m/s. Although a larger standard deviation also increases the rmse, AROME Arctic still has

193 smaller rmse values than the global systems throughout the entire one-year period. Interestingly,
194 the rmse values of HRES and ENS are very similar, although the models have different horizontal
195 and vertical resolutions. ERA-Interim has the largest rmse throughout the entire year. In Figure 7
196 the spatial maps of wind rmse and bias of AROME Arctic and HRES are shown for the wintertime.
197 In the region of the Svalbard Archipelago the wind rmse is smaller by about 1 m/s for HRES
198 and further, the wind bias for HRES is generally negative (-1 - -3 m/s), whereas it is positive
199 for AROME Arctic (1-3 m/s). The coastal areas at the Norwegian mainland show the largest
200 differences between AROME Arctic compared to HRES, for both rmse and bias, with differences
201 of about 2 m/s. Again, the wind bias for HRES is mainly negative, whereas AROME Arctic shows
202 positive and negative values.

203 *b. Upper air*

204 We analyse observational records from three radiosonde sounding stations, which are all located
205 within the AROME Arctic model domain. Ny Ålesund is the most northward station and located
206 on Svalbard, whereas Bjørnøya is an island between the Svalbard Archipelago and the Norwegian
207 mainland, and Jan Mayen is an island between Iceland and Svalbard. The three weather stations
208 are marked by green dots in Figure 1. The radiosonde data is not independent, in the sense that it
209 is assimilated in all of the evaluated model systems.

210

211 In the following, we are presenting two separate upper-air analyses. First, a pressure-level
212 based verification is performed with pressure levels ranging from 950 to 50 hPa. The observation
213 data has been obtained from the NOAA/ESRL Radiosonde Database (www.esrl.noaa.gov/raobs/).
214 Second, the lowest atmospheric layer (10 - 300 m) is analysed, therefore the raw radiosonde
215 data and the model output are interpolated on a z-level grid for altitudes from 10 to 300 m. All

216 radiosonde data are compared against forecasts of 12 h lead time and analysis times at 0000 and
217 1200 UTC.

218

219 The upper air temperature and wind verification is shown for the two stations, Bjørnøya and
220 Jan Mayen (Figure 8). Below the 50 hPa pressure level the temperature bias for all models is
221 below 0.3 K, whereas ERA Interim has the smallest values in between 300 and 900 hPa. The
222 temperature rmse for all models is around 1 and 2 K for Bjørnøya and Jan Mayen, respectively.
223 The rmse values peak at around 850 and 200 hPa at both weather stations. The upper peak, in the
224 height of the tropopause, is also visible in the analyses of Bromwich et al. (2016). At Jan Mayen
225 all models have very similar rmse and bias values, whereas at Bjørnøya HRES and ENS have
226 smallest rmse values and almost no differences between the models is visible. AROME Arctic
227 has lower rmse values compared to ERA Interim only in the two lowest levels (925 and 1000
228 hPa) at Bjørnøya. In general, for both locations, the largest difference in between the models for
229 temperature rmse and bias are in the levels closest to the surface.

230

231 The similarities between Arome Arctic, HRES and ENS at Jan Mayen are most likely due to
232 the proximity of the (most common inflow) lateral boundaries. The reason for the increased rmse
233 at Bjørnøya should be investigated further. It might be related to the initialization process with
234 3DVAR assimilation in combination with large scale mixing of 6 h old HRES data (Müller et al.
235 2017), the influence from 6 h old lateral boundary conditions from HRES, or the presence of more
236 small scale features typically increasing the rmse.

237

238 The rmse for wind is between 2 and 5 m/s . The rmse peaks at about 300 hPa, which coincides
239 with the height of the strongest upper level winds (average values of around 20 m/s) and the polar

240 jet stream, consistently with the radiosonde verification of Bromwich et al. (2016). All models
241 have very similar rmse values. The wind bias is negative above the lowest level (1000 hPa), with
242 values below 1 m/s. At Bjørnøya ERA Interim has the largest negative bias. Largest differences of
243 wind bias in between the models are in the lowest level (1000 hPa) and for Jan Mayen, all models
244 have a positive bias in the lowest level with values of up to 1.8 m/s.

245

246 The radiosonde verification of the lower 300 m of the atmosphere is shown for the Ny Ålesund
247 station (Figure 9). We are specifically interested in the representation of the stable boundary
248 layer and only include timesteps in the analysis, where the lower 100 meters of the atmosphere
249 is stable stratified. The stability is determined from the observed potential temperature profile.
250 In total, around 250 timesteps are utilized for the analysis. The mean observed and forecasted
251 profiles of temperature and wind show that in the lower 50 m above the surface the mean observed
252 temperature increases slightly with height, which is not visible in the models' forecasts (Figure 9).
253 The temperature bias is smallest for AROME Arctic (around 0.5 K) and largest for ERA Interim
254 (up to 2 K). The temperature rmse of all the models is largest in the lower 50-100 m with values
255 of up to 2 K, whereas in heights of 100 to 300 m the rmse is about 1 K smaller.

256

257 The shape of the mean wind profile of AROME Arctic is similar to the observed, but with a
258 positive bias of around 1 m/s. The mean observed boundary layer thickness is about 100 m. In
259 AROME Arctic this seems to be well represented, however, in all the global models the boundary
260 layer thickness is much larger with about 300 meter, or even thicker. This is an indication of a too
261 diffusive boundary layer in the ECMWF models (Viterbo et al. 1999; Beljaars 2001). The wind
262 bias of the ECMWF models is in between 0 and 2 m/s in the lower 300 m of the atmosphere. The
263 wind rmse for all models increases with height and is 3 and 4 m/s in all models.

264 **4. Representation of a polar low and strong winds**

265 In addition to the rmse and bias verification in the previous section, an important characteristic
266 of a forecasting system is the ability to predict high-impact weather conditions. In the European
267 Arctic polar lows are frequently observed. They develop over open sea (e.g. Blechschmidt 2008;
268 Noer et al. 2011) and, although they dissipate quickly after landfall, their small scale and fast
269 development often put human life and property, as well as the natural environment, at great risk.

270

271 CAOs, polar lows, and in general the largest wind variability and maxima are observed in
272 winter months (Figure 3). Hence, before we analyse one specific polar low case in the Norwegian
273 Sea, we first compare the spatial distribution of the 95th percentile wind speed (P95) in between
274 all analysed model systems (Figure 10). It shows that wind extremes are largest in AROME
275 Arctic with P95 values of up to 20 m/s. The ECMWF models show P95 values below 20 m/s
276 and, in general, the global models have very similar characteristics despite their different spatial
277 resolutions. Most pronounced differences between AROME Arctic and the ECMWF models are
278 in coastal areas of the Norwegian mainland and over Svalbard, where AROME Arctic has values
279 of up to 20 m/s and the ECMWF systems have values of 10 m/s and below. Over the ocean areas,
280 in the northern part of the Norwegian Sea and along the Novaya Zemlya Island the model systems
281 are different in their representation of high wind speeds, as well. There, AROME Arctic shows
282 again values of up to 20 m/s, while the ECMWF systems have values of around 15 m/s.

283

284 On 8 December 2016 a low formed northeast of Jan Mayen, and intensified as it moved
285 south-eastwards toward the coast of Finnmark in Northern Norway. The low was initially not
286 termed a polar low since the airmass in which it formed was not very unstable. Soundings only

287 showed instability up till approximately 700 hPa, whereas 500-400 hPa is regarded as the normal
288 for polar lows. There were instead several other dynamical factors involved: The polar low
289 developed from an open wave that was embedded in a northwesterly jet flowing across Greenland,
290 and in a later stage it exited the jet on the cold north side (left jet exit, Brümmer et al. 2009). This
291 is a formation pattern that favors rapid intensification. Furthermore, it followed a sharp baroclinic
292 zone at the southwestern edge of an upper cold core throughout its lifespan. Only at the time of
293 landfall (between 1800 to 2400 UTC) it arrived into an area of deeper instability, and there it took
294 on the shape of a large polar low.

295

296 A visual comparison of forecasted winds in between the AROME Arctic and HRES shows
297 that the forecasted polar low location (lead time 30 h) of the two systems is very similar and is
298 consistent with satellite observations (not shown). In order to analyse the wind characteristics of
299 the model systems we compare wind speeds of the very short-range forecasts (6 h lead time) of
300 AROME Arctic and HRES with the the Advanced Scatterometer (ASCAT) level 2 wind product
301 (Figure 11). Two satellite passages of the ASCAT winds are shown, which are approximately
302 1 h apart. The wind patterns associated with the polar low, are well represented in both model
303 systems. Note, both model systems assimilate ASCAT winds.

304

305 Because of the mix of dynamical forcing (left jet exit) the low caused very strong winds on
306 the Norwegian mainland. The synoptic observations from Fruholmen lighthouse at the Finnmark
307 coast gave 10 m sustained winds of 29 m/s with gusts of 37 m/s. This makes this low one of the
308 5% strongest polar lows recorded since 2000. Maximum observed wind speeds associated with
309 this polar low and along the Norwegian coast were about 25 to 30 m/s. A comparison between
310 AROME Arctic and HRES shows that the landfall location, i.e. areas of largest windspeeds, is well

311 predicted by both models (Figure 12). For HRES wind speeds are generally underestimated and
312 only at a few locations larger than 20 m/s. In AROME Arctic the maximum wind speeds along
313 the coast are consistent with the observations. Further inland, AROME Arctic underestimates,
314 however, shows still more consistent results than HRES.

315 **5. Challenges in the surface representation**

316 In AROME Arctic the largest part of the model domain is covered by ocean and sea-ice. In
317 the following, we discuss the state-of-the-art of describing sea-ice and ocean characteristics
318 in (convective-scale) Arctic weather prediction systems, and further, highlight some important
319 features which are currently not available.

320

321 Sea-ice is described in AROME Arctic by using satellite sea-ice concentration from the
322 OSI-SAF satellite product (Rasmus et al. 2016). The effective resolution of this data is about
323 10-20 km. While the sea-ice temperature is dynamically modelled by a 1D sea-ice model, the
324 sea-ice concentration stays constant during the forecast (Batrak et al. 2017). Furthermore, the
325 representation of sea-ice concentration in the model does not allow for small-scale structures
326 in the sea-ice (e.g. sea-ice leads) but rather represents smoothed sea-ice characteristics, as for
327 example illustrated in Figure 13.

328

329 The representation of sea-ice leads is specifically important in the Marginal Ice Zone (MIZ)
330 and multi-annual statistics show that sea-ice lead frequencies are largest in the areas of the Fram
331 Strait and Barents Sea (Willmes and Heinemann 2016). The sea-ice conditions, at the start of
332 and during (after 4 days) a CAO event in March 2016, are illustrated by the OSI-SAF sea-ice
333 concentration product, by the MODIS instrument based satellite product of sea-ice leads (Willmes

334 and Heinemann 2015), and by a mosaic of Synthetic Aperture Radar (SAR) images. The latter is
335 a novel product from the European satellites Sentinel-1 A and B and 43 scenes with SAR data in
336 HV-polarization obtained in Extra Wide mode with spatial resolution of 100 m was downloaded
337 from the Copernicus Open Access Hub for two periods of times: 18, 19 March 2016 and 23, 24
338 March 2016. Calibration of normalized radar cross-section and removal of thermal and scalloping
339 noise from SAR data was performed using the method developed by (Park et al. 2017). A mosaic
340 of SAR images on a regular grid in geographic projection was created using open-source Nansat
341 software (Korosov et al. 2016).

342

343 During the CAO a large-scale drift of the sea-ice cover in southward (south-westward) direction
344 towards the Svalbard Archipelago is visible in all products (Figure 13). Also, the OSI-SAF sea-ice
345 drift product (Lavergne 2016) shows a southward sea-ice drift of more than 10 km per day (not
346 shown). The sea-ice lead structure, as seen in the MODIS product, shows large sea-ice leads (or
347 openings) of O(10 - 100 km), which quickly change their characteristic structure during the CAO.
348 A consistent structure of leads and their changes is also visible in the SAR images. Apparently,
349 sea-ice leads are dominant in the entire domain shown in Figure 13 and not only in the MIZ. We
350 conclude that those sea-ice lead structures and the dynamics on short time-scales are relevant for a
351 2.5 kilometer resolution atmospheric model. The fast changes of sea-leads, induced by the strong
352 winds during CAOs, might provide for an important feedback mechanism to the atmosphere, due
353 to the associated changes in air-sea heat fluxes. The MODIS sea-ice lead product is based on the
354 thermal-infrared data of the MODIS sensor and the leads are identified by comparing the warm
355 signature of the ocean (lead) in comparison to the colder thick and snow-covered sea-ice. Thus,
356 this strongly highlights the modified ocean heat fluxes in areas of sea-ice leads.

357

358 Sea surface temperature (SST) ranges from 0 to 8°C in the AROME Arctic domain and
359 shows fine structures and strong gradients. This is a result of the extension of the warm North
360 Atlantic Current, which transports warm water masses towards high latitudes. Those structures
361 are smoothed in the currently used satellite retrievals (Figure 14). Higher resolution products
362 are currently only available from high-resolution ocean prediction systems. Although the spatial
363 structures of high-resolution models are more realistic, e.g. the eddying recirculation of Atlantic
364 water along the sea-ice edge (Hattermann et al. 2016), there are relatively large biases due to the
365 lack of observational data on small spatial scales (Figure 14).

366

367 In order to test the impact of the high-resolution representation of the ocean surface temperature
368 on the model performance, we performed a model sensitivity experiment, where SST and sea ice
369 concentration is initialized by an operational ocean forecasting system. The ocean system has
370 a horizontal resolution of 4 km and is based on the ROMS model framework (Shchepetkin and
371 McWilliams 2005; Debernard et al. 2017). The sensible heat fluxes, during the CAO described
372 in the previous paragraphs of this section, with high-resolution and coarser resolution SST are
373 shown in Figure 14. As expected the heat fluxes show variations on higher spatial scales. In
374 general, however, the use of the ROMS SST and sea-ice concentration fields in the atmospheric
375 forecasting system is leading to a degradation of the temperature forecasts compared to the op-
376 erational system (not shown). We conclude that the bias of the simulated SST dominates, and
377 thus, limits the expected improvements from the representation of ocean meso-scale characteris-
378 tics. High-quality high-resolution SST data from satellites will be needed in the future, in order to
379 provide the atmospheric model with SST data directly, or indirectly via a constrained ocean model
380 system.

381 **6. Summary and conclusion**

382 A detailed analysis of the representation of wind and temperature is performed with the regional
383 convection-allowing model system AROME Arctic, as well as, with different configurations
384 (HRES, ENS and ERA-Interim) of the global model system ECMWF IFS. Surface observations
385 are from the Norwegian weather station network which cover Northern Norway, the Svalbard
386 Archipelago, and some islands in the Nordic Seas. The evaluation of the atmosphere above
387 10 m altitude is performed at three radiosonde observation sites. The focus of this study is
388 on the summarized statistics of very short-range forecasts and without a detailed analysis on
389 dependencies on the forecast range.

390

391 In general rmse values are largest during winter months, when the variability of winds and
392 temperature is highest. The main improvement of the convective-scale model system, compared
393 to the global ones, is found at the surface and in the representation of the stable boundary layer. At
394 the surface AROME Arctic has a reduced bias and rmse compared to the global model systems.
395 Those improvements are mainly visible on the Norwegian mainland, while the forecast skill of
396 AROME Arctic and HRES is similar on the Svalbard Archipelago. The observed boundary layer
397 thickness during stable atmospheric conditions is best represented by AROME Arctic, while
398 the ECMWF models have a too diffusive turbulence closure model which results in too deep
399 boundary layers (Viterbo et al. 1999; Beljaars 2001). The upper air evaluation shows that all
400 model system have similar characteristics in heights of 950 to 50 hPa.

401

402 Furthermore, the forecasts of a single polar low are analysed. AROME Arctic shows clear
403 improvements in forecasting the land-fall of a polar low and the associated extreme winds over

404 the ocean and in coastal areas (up to 30 m/s). It shows that HRES underestimates the coastal
405 extreme wind speeds during the land-fall of the analysed polar low. However, AROME Arctic,
406 HRES, and ENS have similar skill, despite their different vertical and horizontal resolution, in
407 forecasting the location of a polar low, which is identified by a visual comparison of mean sea
408 level pressure and ASCAT wind data.

409

410 The performed evaluation of the model systems has some limitations. The observation network
411 in the northern part of the analysed domain and over the ocean and sea-ice covered areas is sparse,
412 which implies that a generalization of the results is difficult. Most of the surface observation
413 stations are on the Norwegian mainland and thus, they might dominate some of the summary
414 statistics. Furthermore, the surface observations are not assessed individually, i.e. it could be of
415 interest for future studies to classify specific observing stations, for example with respect to the
416 station's representativeness, land-sea mask (model vs reality), and physiography. The wind bias
417 of the AROME Arctic model system compared to HRES showed some important differences in
418 between the Svalbard Archipelago and Norwegian mainland. It would be interesting for future
419 studies to further analyse and understand the positive wind bias of the high-resolution model in
420 the norther part of the domain. Also, it will be of interest to include more variables than wind and
421 temperature, e.g. humidity, cloud cover, and precipitation. Verification of precipitation forecasts
422 would imply a careful use of snow-correction schemes and spatial verification methods, which
423 will be part of future studies.

424

425 As a main challenge for convective-scale atmospheric modelling in the European Arctic, the
426 representation of the ocean and sea-ice conditions, are identified. Generally, sea-ice initialization
427 is a major issue for weather prediction (Smith et al. 2016) and the sea-ice characteristics are a

428 dominant constraint for atmospheric surface fluxes (Bourassa et al. 2013). The kilometer-scale
429 structures of the sea-ice can have strong effects on atmospheric conditions on short-time scales
430 such as storm development and extreme convective events (Valkonen et al. 2008; Vihma 2014).
431 Lüpkes et al. (2008) analysed the effect of sea-ice leads on the surface atmospheric boundary layer,
432 by using a 1D atmospheric model coupled to a thermodynamic sea-ice model. They concluded
433 that under clear skies in winter a 1% change in the sea-ice concentration can increase the T10M
434 by up to 3.5 K. In an operational context sea-ice lead products are not available in real-time and
435 with a sufficient quality. However, developments of satellite-based information on sea-ice leads
436 (Röhrs and Kaleschke 2012; Willmes and Heinemann 2015) and novel high-resolution sea-ice
437 model approaches (Rampal et al. 2016; Wang et al. 2016) are promising. Hence, we can expect
438 significant advances in the realism of the sea-ice representation for convective scale weather
439 prediction in the near-future.

440

441 Also the SST products which are currently available are too coarse and do not represent the
442 ocean small- and meso-scale characteristics. There are also gridded high-resolution products
443 available, however, with a significant amount of missing values due to cloud contamination.
444 Thus, important small-scale feature with large temperature gradients are missing in the SST
445 fields, which are available for operational weather prediction. New satellite-based SST products
446 will be soon available (e.g. from Sentinel 3 Sea and Land Surface Temperature Radiometer;
447 www.sentinel.esa.int) and possibly a combination of the existing SST products could result
448 in continuous high-resolution product, which could be used to assess their benefits for weather
449 forecasting.

450

451 The improved sea-ice and ocean surface representation will be specifically important during
452 CAOs, where the small scale sea-ice characteristics change quickly due to strong winds. Further-
453 more, during CAOs air-sea fluxes are largest due to the strong winds and large difference between
454 the ocean and the cold atmospheric temperature. Thus, an improved representation of ocean and
455 sea-ice will presumably improve forecasts and important dynamical features of CAOs, which can
456 have an important benefit for downstream weather conditions, such as the development of polar
457 lows and even mid-latitude weather.

458

459 *Acknowledgments.* We thank Eivind Støylen for the operational handling of the AROME Arc-
460 tic model system. Further, we thank Sascha Willmes and Günther Heinemann for the extension
461 of their daily pan-Arctic sea-ice lead maps to the year 2016. We acknowledge the helpful and
462 constructive comments and suggestions from Thomas Lavergne, David Bromwich and two anonym-
463 ous reviewers.

464 **References**

- 465 Atlaskin, E., and T. Vihma, 2012: Evaluation of NWP results for wintertime nocturnal boundary-
466 layer temperatures over Europe and Finland. *Q. J. R. Meteorol. Soc.*, **138** (667), 1440–1451,
467 doi:10.1002/qj.1885.
- 468 Batrak, Y., E. Kourzeneva, and M. Homleid, 2017: Implementation of a simple thermodynamic
469 sea ice scheme within the ALADIN-HIRLAM numerical weather prediction system. (*subm.*).
- 470 Bauer, P., L. Magnusson, J.-N. Thpaut, and T. M. Hamill, 2016: Aspects of ECMWF model
471 performance in polar areas. *Q. J. R. Meteorol. Soc.*, **142** (695), 583–596, doi:10.1002/qj.2449.
- 472 Bauer, P., and Coauthors, 2013: Model cycle 38r2: Components and performance. ECMWF Tech-
473 nical Memorandum 704, European Centre for Medium-Range Weather Forecasts, Reading, UK.
474 URL http://old.ecmwf.int/publications/library/ecpublications/_pdf/tm/701-800/tm704.pdf.
- 475 Beljaars, A. C. M., 2001: Issues in boundary layer parametrization for large scale mod-
476 els. ECMWF seminar on: Key issues in the parametrization of subgrid physical processes,,
477 ECMWF.
- 478 Bengtsson, L., and Coauthors, 2017: The HARMONIE-AROME Model Configuration in
479 the ALADIN-HIRLAM NWP System. *Mon. Wea. Rev.*, **145** (5), 1919–1935, doi:10.1175/
480 MWR-D-16-0417.1.
- 481 Blechschmidt, A.-M., 2008: A 2-year climatology of polar low events over the Nordic Seas from
482 satellite remote sensing. *Geophys. Res. Lett.*, **35** (L09815), doi:10.1029/2008GL033706.
- 483 Bourassa, M. A., and Coauthors, 2013: High-latitude ocean and sea ice surface fluxes:
484 Challenges for climate research. *Bull. Amer. Meteor. Soc.*, **94** (3), 403–423, doi:10.1175/
485 BAMS-D-11-00244.1.

- 486 Bromwich, D. H., A. B. Wilson, L.-S. Bai, G. W. K. Moore, and P. Bauer, 2016: A comparison
487 of the regional Arctic System Reanalysis and the global ERA-Interim Reanalysis for the Arctic.
488 *Q. J. R. Meteorol. Soc.*, **142** (695), 644–658, doi:10.1002/qj.2527.
- 489 Brümmer, B., G. Müller, and G. Noer, 2009: A polar low pair over the Norwegian Sea. *Mon. Wea.*
490 *Rev.*, **137** (8), 2559–2575, doi:10.1175/2009MWR2864.1.
- 491 Davies, H. C., 1976: A lateral boundary formulation for multi-level prediction models. *Q. J. R.*
492 *Meteorol. Soc.*, **102** (432), 405–418, doi:10.1002/qj.49710243210.
- 493 Debernard, J., N. Kristensen, S. Maartensson, K. Wang, and G. Waagb, 2017: metno/metroms:
494 Intermediate release [data set]. Zenodo., Norwegian Meteorological Institute. doi:<http://doi.org/10.5281/zenodo.290667>.
- 495
- 496 Dee, D. P., and Coauthors, 2011: The ERA-Interim reanalysis: configuration and performance of
497 the data assimilation system. *Q. J. R. Meteorol. Soc.*, **137** (656), 553–597, doi:10.1002/qj.828.
- 498
- 499 Donlon, C. J., M. Martin, J. Stark, J. Roberts-Jones, E. Fiedler, and W. Wimmer, 2012: The Oper-
500 ational Sea Surface Temperature and Sea Ice Analysis (OSTIA) system. *Remote Sens. Environ.*,
500 **116** (0), 140 – 158.
- 501
- 502 Emmerson, C., and G. Lahn, 2012: Arctic opening: Opportunity and risk in the high north.
502 *Chatham House-Lloyd's Risk Insight Report*.
- 503
- 504 Gutjahr, O., G. Heinemann, A. Preusser, S. Willmes, and C. Drue, 2016: Sensitivity of ice pro-
505 duction estimates in Laptev Sea polynyas to the parameterization of subgrid-scale sea-ice inho-
505 mogeneities in COSMO-CLM. *Cryosphere Discuss.*, **137**.
- 506
- 507 Hattermann, T., P. E. Isachsen, W.-J. von Appen, J. Albretsen, and A. Sundfjord, 2016: Eddy-
507 driven recirculation of Atlantic Water in the Fram Strait. *Geophys. Res. Lett.*, **43** (7).

- 508 Hines, K. M., and D. H. Bromwich, 2017: Simulation of late summer Arctic clouds during ASCOS
509 with Polar WRF. *Mon. Wea. Rev.*, **145**, 521–541, doi:10.1175/MWR-D-16-0079.1.
- 510 Jung, T., and M. Leutbecher, 2007: Performance of the ECMWF forecasting system in the Arctic
511 during winter. *Q. J. R. Meteorol. Soc.*, **133** (626), 1327–1340, doi:10.1002/qj.99.
- 512 Jung, T., and M. Matsueda, 2016: Verification of global numerical weather forecasting systems in
513 polar regions using TIGGE data. *Q. J. R. Meteorol. Soc.*, **142** (695), 574–582, doi:10.1002/qj.
514 2437.
- 515 Jung, T., and Coauthors, 2016: Advancing polar prediction capabilities on daily to seasonal time
516 scales. *Bull. Amer. Math. Soc.*, **97** (9), 1631–1647, doi:10.1175/BAMS-D-14-00246.1.
- 517 Korosov, A., M. W. Hansen, K.-F. Dagestad, and A. Yamakava, 2016: Nansat: a scientist-
518 orientated python package for geospatial data processing. *J. Open Res. Softw.*, **4** (1), doi:
519 DOI:<http://doi.org/10.5334/jors.120>.
- 520 Lavergne, T., 2016: Low resolution sea ice drift product user's manual. Tech. rep., Norwegian
521 Meteorological Institute. URL <http://osisaf.met.no/docs/>.
- 522 Lüpkes, C., T. Vihma, G. Birnbaum, and U. Wacker, 2008: Influence of leads in sea ice on the
523 temperature of the atmospheric boundary layer during polar night. *Geophys. Res. Lett.*, **35** (3),
524 doi:10.1029/2007GL032461, l03805.
- 525 Moore, G. W. K., D. H. Bromwich, A. B. Wilson, I. Renfrew, and L. Bai, 2016: Arctic System
526 Reanalysis improvements in topographically-forced winds near Greenland. *Q. J. R. Meteorol.
527 Soc.*, **142**, 2033–245, doi:10.1002/qj.2798.
- 528 Müller, M., and Coauthors, 2017: AROME - MetCoOp : A Nordic convective scale operational
529 weather prediction model. *Wea. Forecasting*, **32**, 609627, doi:10.1175/WAF-D-16-0099.1.

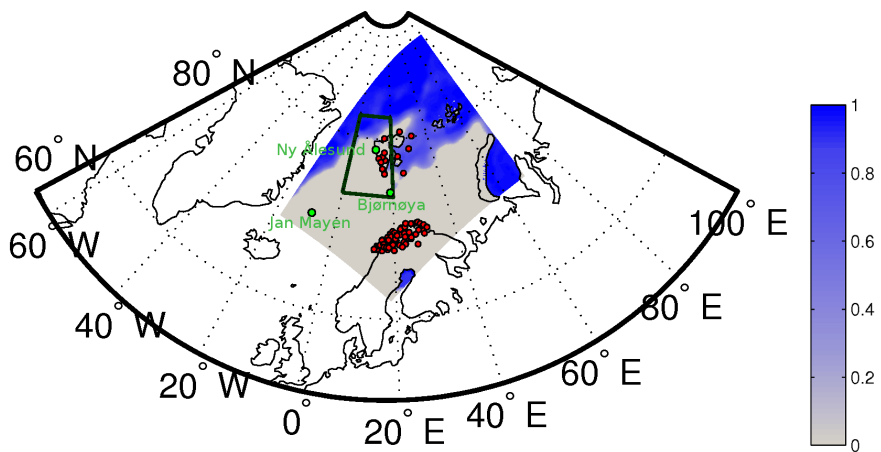
- 530 Noer, G., O. Saetra, T. Lien, and Y. Gusdal, 2011: A climatological study of polar lows in the
531 Nordic Seas. *Q. J. R. Meteorol. Soc.*, **137**, 1762–1772.
- 532 Papritz, L., S. Pfahl, H. Sodemann, and H. Wernli, 2015: A climatology of cold air outbreaks and
533 their impact on airsea heat fluxes in the high-latitude South Pacific. *J. Climate*, **28** (1), 342–364,
534 doi:10.1175/JCLI-D-14-00482.1.
- 535 Park, J.-W., A. Korosov, M. Babiker, S. Sandven, and J. Won, 2017: Efficient thermal noise
536 removal for Sentinel TOPSAR cross-polarisation channel. *IEEE TGRS (in press)*.
- 537 Rampal, P., S. Bouillon, E. Ólason, and M. Morlighem, 2016: neXtSIM: a new Lagrangian sea ice
538 model. *The Cryosphere*, **10**, 1055–1073, doi:doi:10.5194/tc-10-1055-2016.
- 539 Rasmus, T., L. John, P. R.-Helge, and H. Eva, 2016: Product user manual for OSI SAF global sea
540 ice concentration. Tech. rep., Danish Meteorological Institute.
- 541 Röhrs, J., and L. Kaleschke, 2012: An algorithm to detect sea ice leads by using AMSR-E passive
542 microwave imagery. *The Cryosphere*, **6**, 343–352, doi:10.5194/tc-6-343-2012.
- 543 Seity, Y., P. Brousseau, S. Malardel, G. Hello, P. Bnard, F. Bouttier, C. Lac, and V. Masson, 2010:
544 The AROME-France convective-scale operational model. *Mon. Wea. Rev.*, **139** (3), 976–991,
545 doi:10.1175/2010.
- 546 Shchepetkin, A. F., and J. C. McWilliams, 2005: The Regional Ocean Modeling System (ROMS):
547 A split-explicit, free-surface, topography-following coordinate ocean model. *Ocean Modell.*, **9**,
548 347–404.
- 549 Smirnova, J., and P. Golubkin, 2017: Comparing polar lows in atmospheric reanalyses: Arc-
550 tic System Reanalysis versus ERA-Interim. *Mon. Wea. Rev.*, **145**, 2375–2383, doi:10.1175/
551 MWR-D-16-0333.1.

- 552 Smith, G. C., and Coauthors, 2016: Sea ice forecast verification in the Canadian Global Ice Ocean
553 Prediction System. *Q. J. R. Meteorol. Soc.*, **142** (695), 659–671, doi:10.1002/qj.2555.
- 554 Valkonen, T., T. Vihma, and M. Doble, 2008: Mesoscale modeling of the atmosphere over Antarc-
555 tic sea ice: A late-autumn case study. *Mon. Wea. Rev.*, **136** (4), 1457–1474.
- 556 Vihma, T., 2014: Effects of Arctic sea ice decline on weather and climate: A review. *Surv. Geo-
557 phys.*, **35** (5), 11751214.
- 558 Vihma, T., and Coauthors, 2014: Advances in understanding and parameterization of small-scale
559 physical processes in the marine Arctic climate system: a review, , 14, 9403-9450. *Atmos. Chem.*
560 *Phys.*, **14** (17), 9403–9450, doi:10.5194/acp-14-9403-2014.
- 561 Viterbo, P., A. Beljaars, J.-F. Mahfouf, and J. Teixeira, 1999: The representation of soil moisture
562 freezing and its impact on the stable boundary layer. *Quart. J. Roy. Meteorol. So.*, **125** (559),
563 2401–2426, doi:10.1002/qj.49712555904.
- 564 Wang, Q., S. Danilov, T. J. Kaleschke, and A. Wernecke, 2016: Sea ice leads in the Arctic Ocean:
565 Model assessment, interannual variability and trends. *Geophys. Res. Lett.*, **43** (13), 7019–7027.
- 566 Willmes, S., and G. Heinemann, 2015: Pan-Arctic lead detection from MODIS thermal infrared
567 imagery. *Ann. Glaciol.*, **56**, 29–37, doi:10.3189/2015AoG69A615.
- 568 Willmes, S., and G. Heinemann, 2016: Sea-ice wintertime lead frequencies and regional charac-
569 teristics in the Arctic, 2003-2015. *Remote Sens.*, **8** (4).
- 570 WMO-PPP, 2013: WWRP Polar Prediction Project Science Plan, No.1. Tech. Rep. 69pp, World
571 Meteorological Organization.

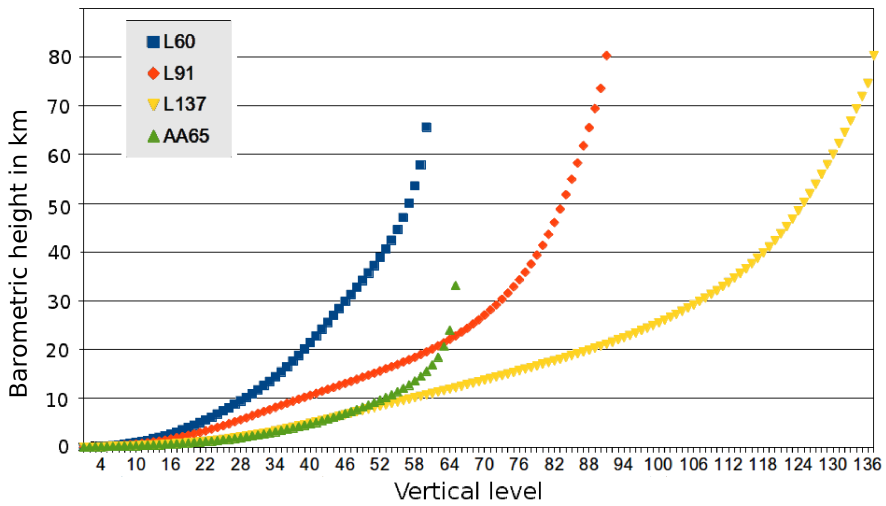
572 Zappa, G., L. Shaffrey, and K. Hodges, 2014: Can polar lows be objectively identified and tracked
573 in the ECMWF operational analysis and the ERA-Interim reanalysis? *Mon. Wea. Rev.*, **142** (8),
574 2596–2608, doi:10.1175/MWR-D-14-00064.1.

575 LIST OF FIGURES

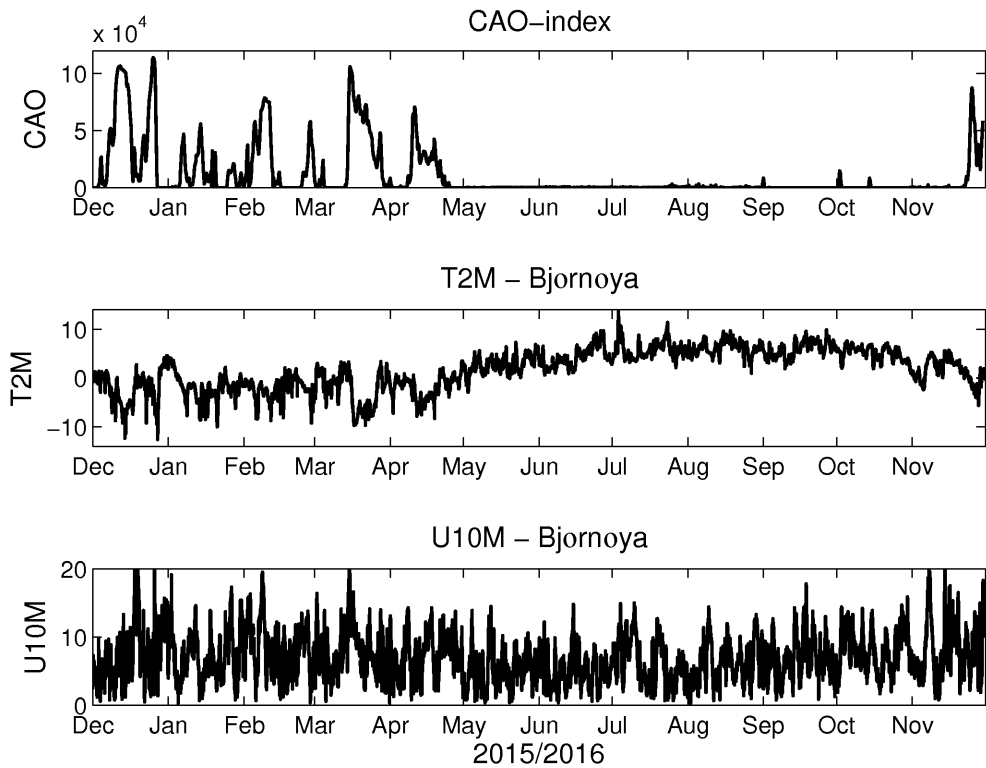
576	Fig. 1. The model domain is shown by a color-contoured field of sea-ice concentration (5 March	31
577	2016). Furthermore, surface observations and radiosondes which are used for the statistical	
578	verification are shown by red and green dots, respectively. The dark-green box indicates the	
579	area used for the CAO index computation.	
580	Fig. 2. The distribution of vertical levels in the forecasting systems. The x-axis is the level-number	32
581	starting with the level closest to the surface. The y-axis represents the standart altimetric	
582	height in km. AA65 refers to the 65 levels of AROME Arctic. L137, L91, and L60 to the	
583	vertical levels of HRES, ENS, and ERA Interim, respectively.	
584	Fig. 3. (Top) The timeseries of the CAO-index (number of grid points in AROME Arctic where the	33
585	CAO index (defined in Papritz et al. (2015)) is larger than 4). The observed T2M (middle)	
586	and U10M (bottom) at the Bjørnøya surface observation site is shown.	
587	Fig. 4. Timeseries (running mean) of the rmse of T2M (top) and U10M (bottom) analysed at 89	34
588	surface observation sites shown in Figure 1. The rmse values of AROME Arctic (magenta),	
589	HRES (red), ENS (blue) and ERA Interim (green) are shown.	
590	Fig. 5. The bias T2M computed for the period (1 December 2015 till 15 March 2016). Results are	35
591	divided into cases, where $T2M < -10^{\circ}\text{C}$ and $T2M > -10^{\circ}\text{C}$, for the AROME Arctic model	
592	in (a) and (c) and the HRES in (b) and (d).	
593	Fig. 6. The rmse T2M computed for the period (1 December 2015 till 15 March 2016). Results are	36
594	divided into cases, where $T2M < -10^{\circ}\text{C}$ and $T2M > -10^{\circ}\text{C}$, for the AROME Arctic model	
595	in (a) and (c) and the HRES in (b) and (d).	
596	Fig. 7. The rmse and bias of U10M computed for the period (1 December 2015 till 15 March 2016)	37
597	for the AROME Arctic model in (a) and (c) and the HRES in (b) and (d)	
598	Fig. 8. The rmse (solid lines) and bias (dashed lines) of upper air evaluation at pressure levels	38
599	between 1000 hPa and 50 hPa. Evaluation is performed for a one-year period and with ra-	
600	diosonde observations from Bjørnøya and Jan Mayen weather stations. The 12 h forecasts of	
601	AROME Arctic (magenta), HRES (red), ENS (blue) and ERA Interim (green) are evaluated	
602	against temperature observations, in (a) and (b), and wind observations, in (c) and (d).	
603	Fig. 9. Evaluation of the lower atmosphere (0 - 300 m altitude) with radiosonde observations from	39
604	the Ny Ålesund weather station. The evaluation is performed during stable atmospheric con-	
605	ditions in the lower 100 m, determined from the observed potential temperature. (Left) the	
606	rmse (solid lines) and bias (dashed lines) for temperature and wind, respectively is shown.	
607	(Right) the mean profiles of temperature (top) and wind (bottom), respectively are shown.	
608	The black solid line represents the observations.	
609	Fig. 10. The 95th percentile of U10M wind in (a) AROME Arctic, (b) HRES, (c) ENS, and (d) ERA	40
610	Interim. The statistics are performed for the time from 1 December 2015 to 30 March 2016.	
611	Fig. 11. Polar low close to the Norwegian coast at 1800 UTC 8 December 2016. (a) The 10 meter	41
612	wind speed of two tracks (approx. 1h apart) from level 2 ASCAT 12.5km resolution product.	
613	(b) and (c) the 6 h forecasts (with analysis time at 1200 UTC 08 December 2016) of 10 meter	
614	wind speed from AROME Arctic and HRES, respectively.	



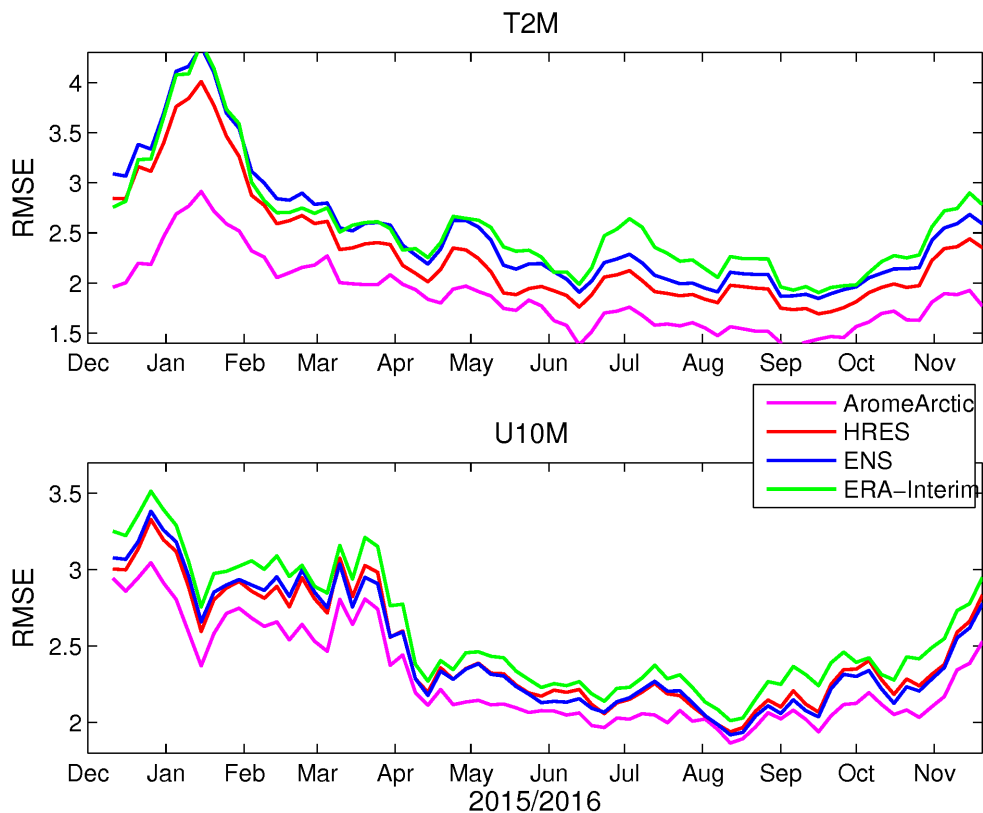
636 FIG. 1. The model domain is shown by a color-contoured field of sea-ice concentration (5 March 2016).
 637 Furthermore, surface observations and radiosondes which are used for the statistical verification are shown by
 638 red and green dots, respectively. The dark-green box indicates the area used for the CAO index computation.



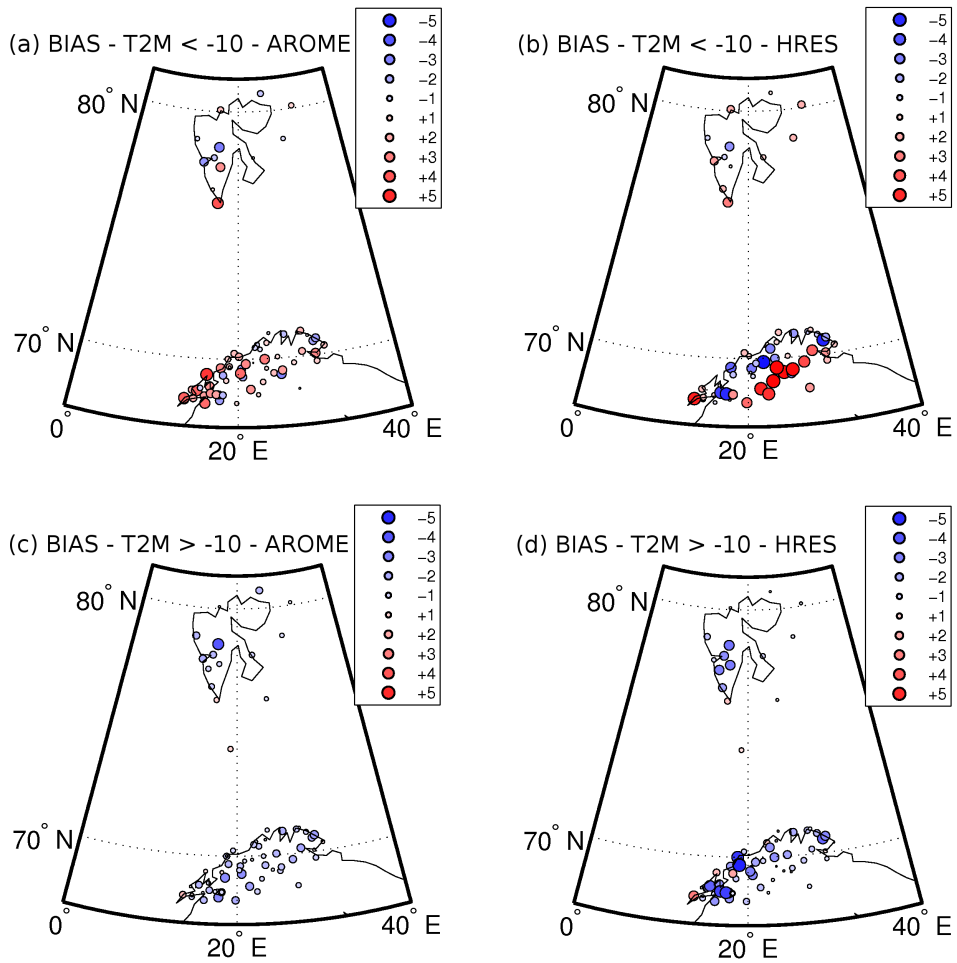
639 FIG. 2. The distribution of vertical levels in the forecasting systems. The x-axis is the level-number starting
 640 with the level closest to the surface. The y-axis represents the standart altimetric height in km. AA65 refers to
 641 the 65 levels of AROME Arctic. L137, L91, and L60 to the vertical levels of HRES, ENS, and ERA Interim,
 642 respectively.



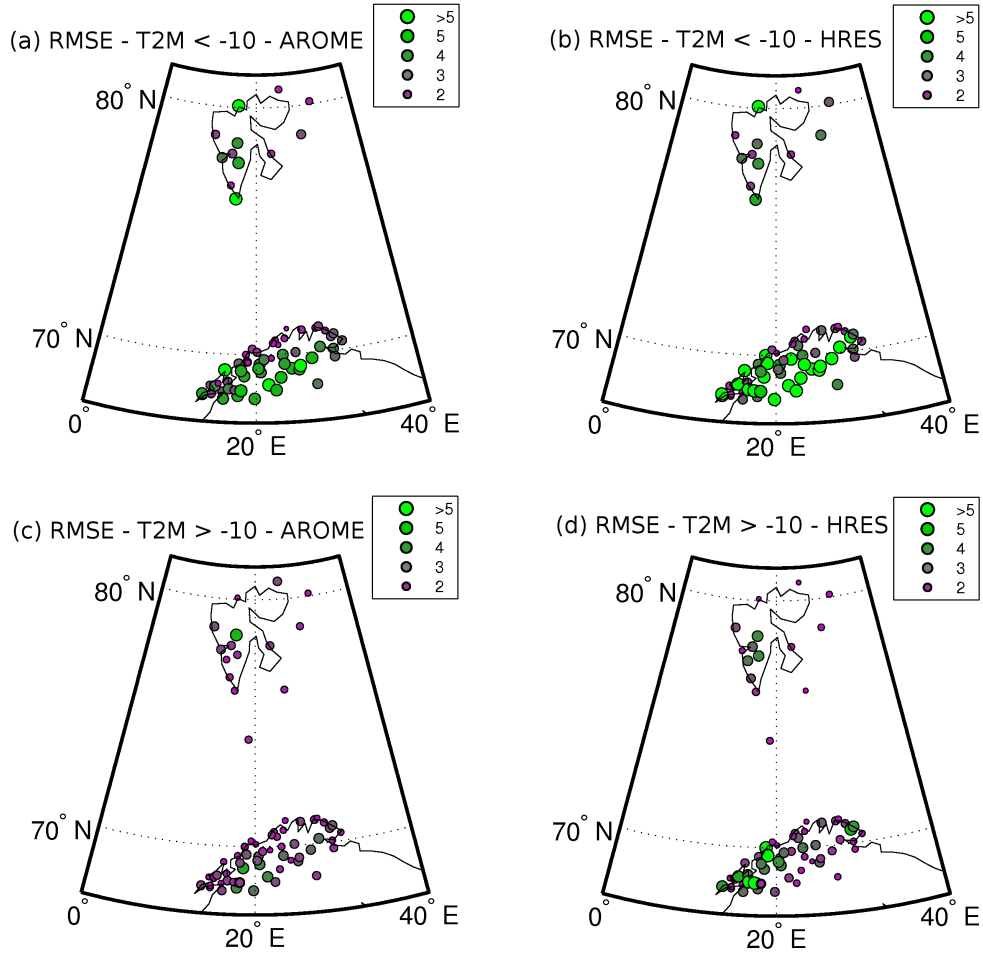
643 FIG. 3. (Top) The timeseries of the CAO-index (number of grid points in AROME Arctic where the CAO
 644 index (defined in Papritz et al. (2015)) is larger than 4). The observed T2M (middle) and U10M (bottom) at the
 645 Bjørnøya surface observation site is shown.



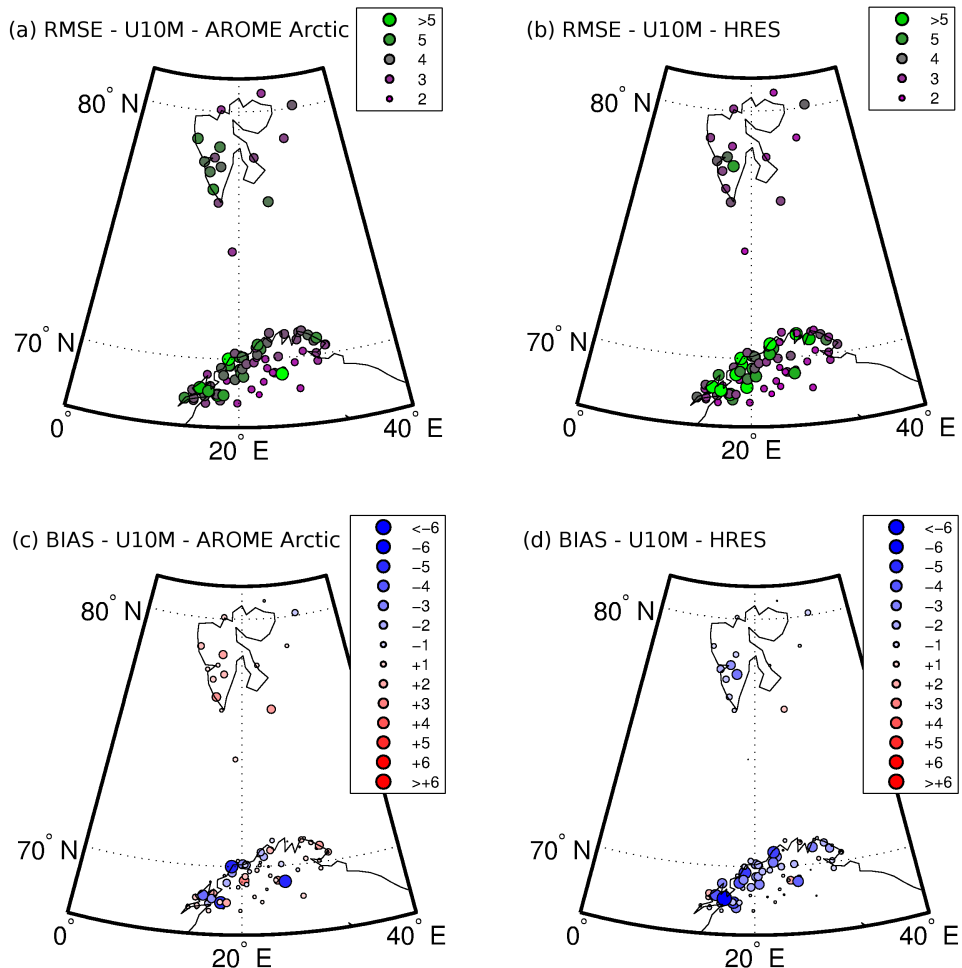
646 FIG. 4. Timeseries (running mean) of the rmse of T2M (top) and U10M (bottom) analysed at 89 surface
 647 observation sites shown in Figure 1. The rmse values of AROME Arctic (magenta), HRES (red), ENS (blue)
 648 and ERA Interim (green) are shown.



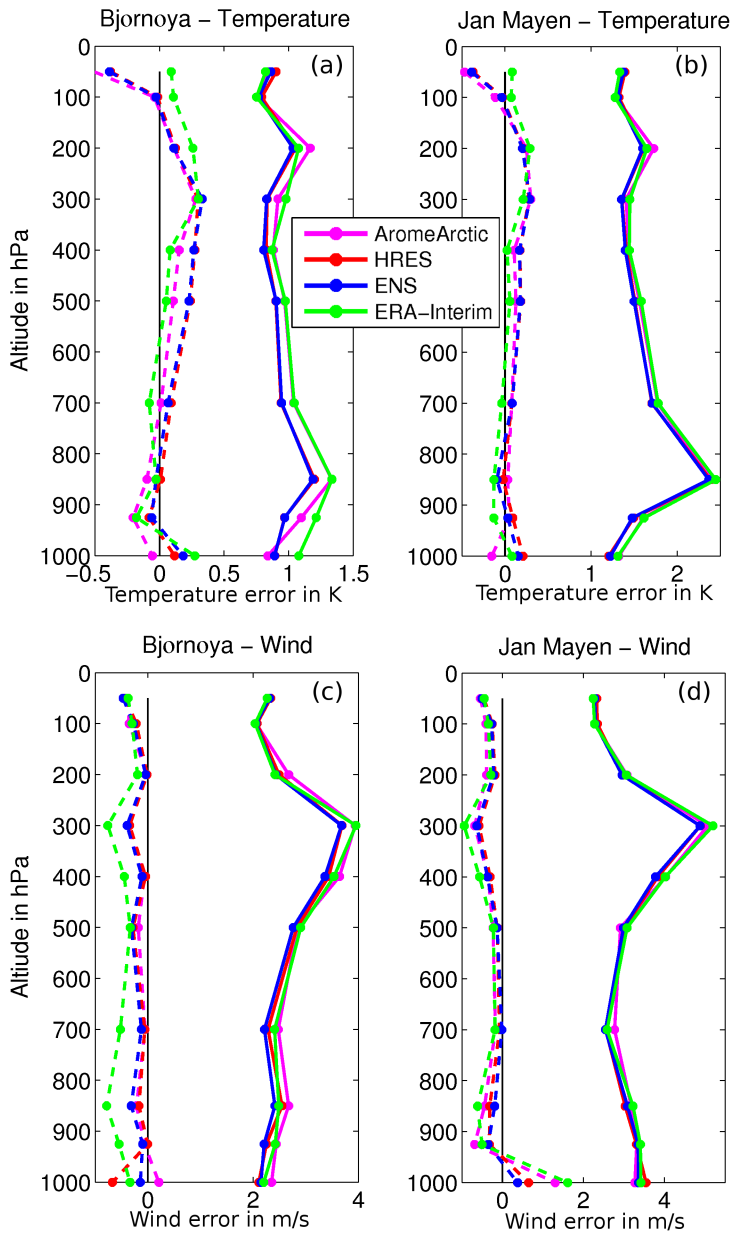
649 FIG. 5. The bias T2M computed for the period (1 December 2015 till 15 March 2016). Results are divided
 650 into cases, where $T2M < -10^{\circ}\text{C}$ and $T2M > -10^{\circ}\text{C}$, for the AROME Arctic model in (a) and (c) and the HRES
 651 in (b) and (d).



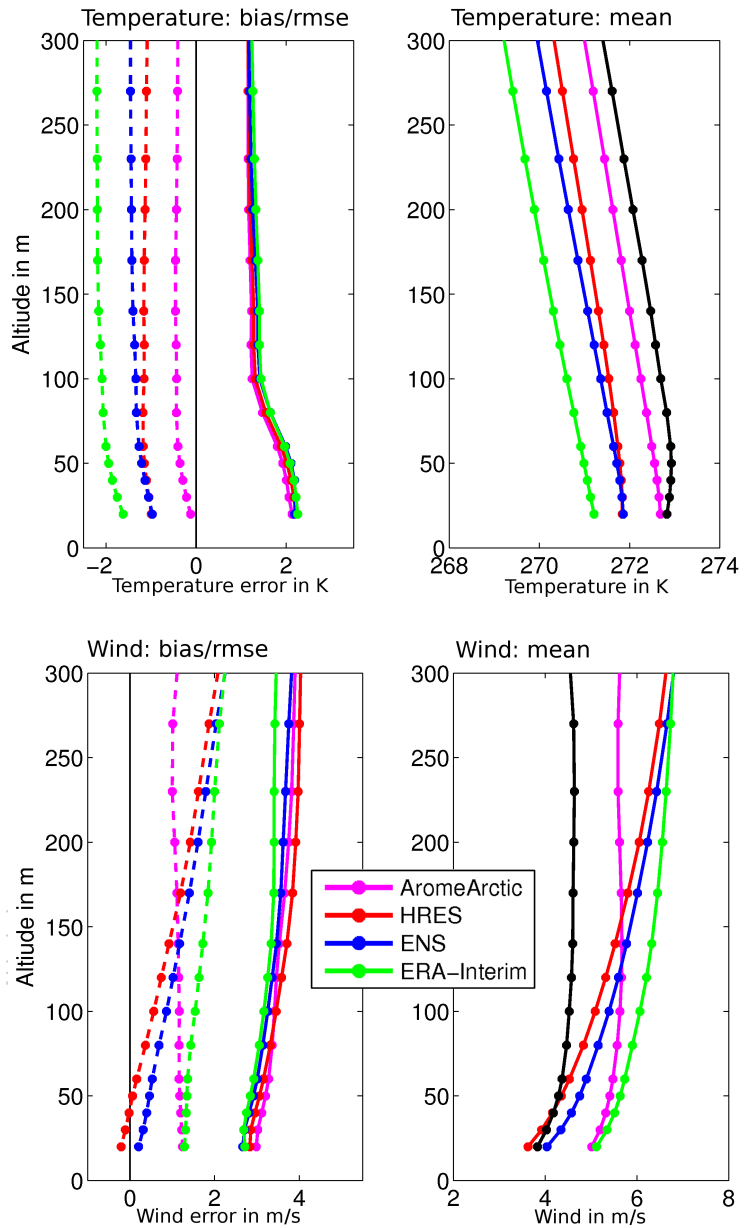
652 FIG. 6. The rmse T2M computed for the period (1 December 2015 till 15 March 2016). Results are divided
 653 into cases, where $T2M < -10^{\circ}\text{C}$ and $T2M > -10^{\circ}\text{C}$, for the AROME Arctic model in (a) and (c) and the HRES
 654 in (b) and (d).



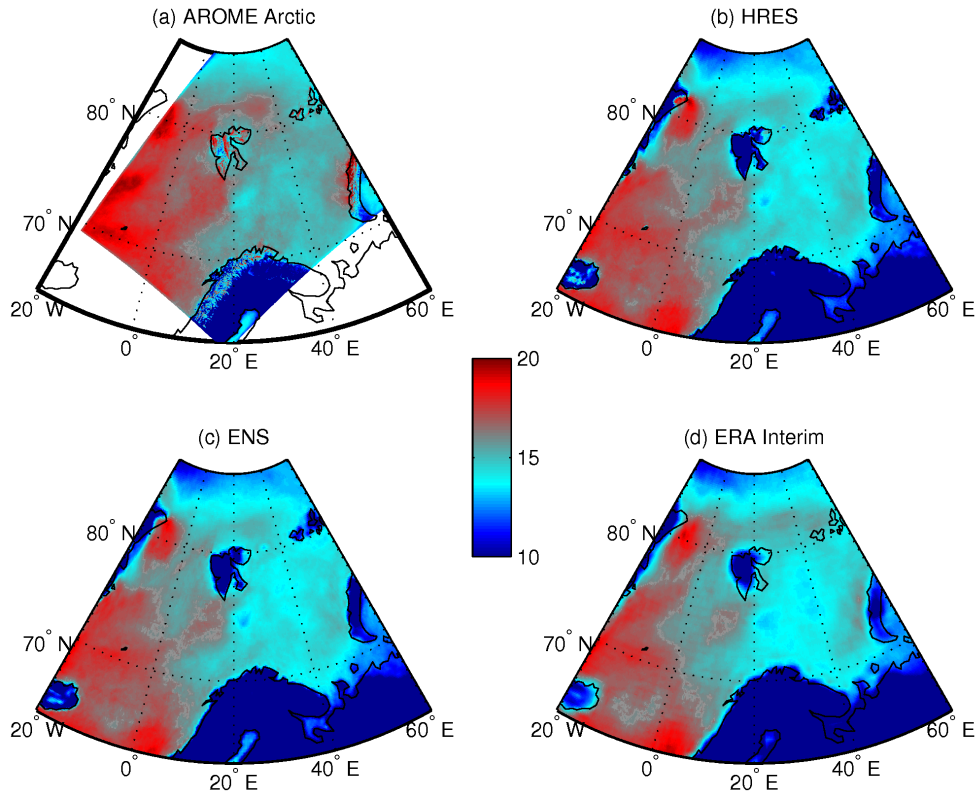
655 FIG. 7. The rmse and bias of U10M computed for the period (1 December 2015 till 15 March 2016) for the
 656 AROME Arctic model in (a) and (c) and the HRES in (b) and (d)



657 FIG. 8. The rmse (solid lines) and bias (dashed lines) of upper air evaluation at pressure levels between 1000
 658 hPa and 50 hPa. Evaluation is performed for a one-year period and with radiosonde observations from Bjørnøya
 659 and Jan Mayen weather stations. The 12 h forecasts of AROME Arctic (magenta), HRES (red), ENS (blue) and
 660 ERA Interim (green) are evaluated against temperature observations, in (a) and (b), and wind observations, in
 661 (c) and (d).

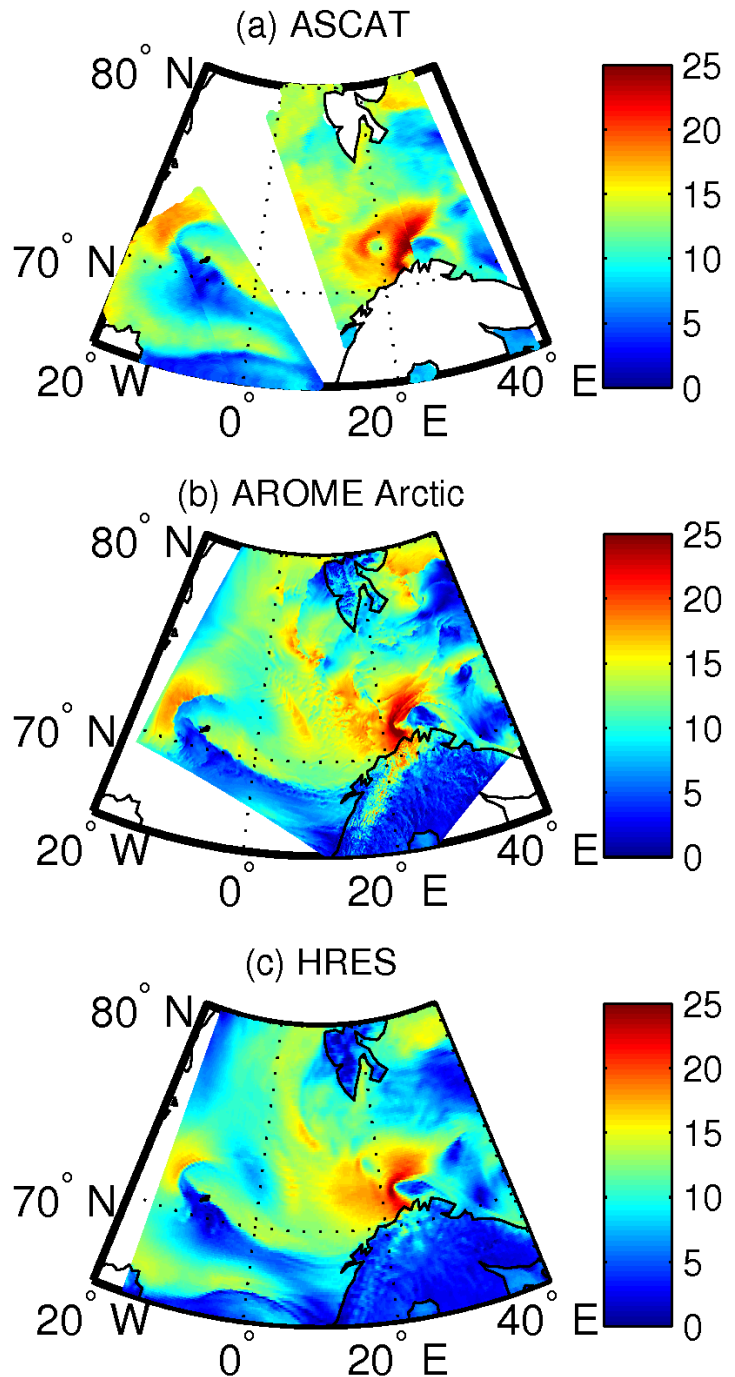


662 FIG. 9. Evaluation of the lower atmosphere (0 - 300 m altitude) with radiosonde observations from the Ny
 663 Ålesund weather station. The evaluation is performed during stable atmospheric conditions in the lower 100
 664 m, determined from the observed potential temperature. (Left) the rmse (solid lines) and bias (dashed lines) for
 665 temperature and wind, respectively is shown. (Right) the mean profiles of temperature (top) and wind (bottom),
 666 respectively are shown. The black solid line represents the observations.

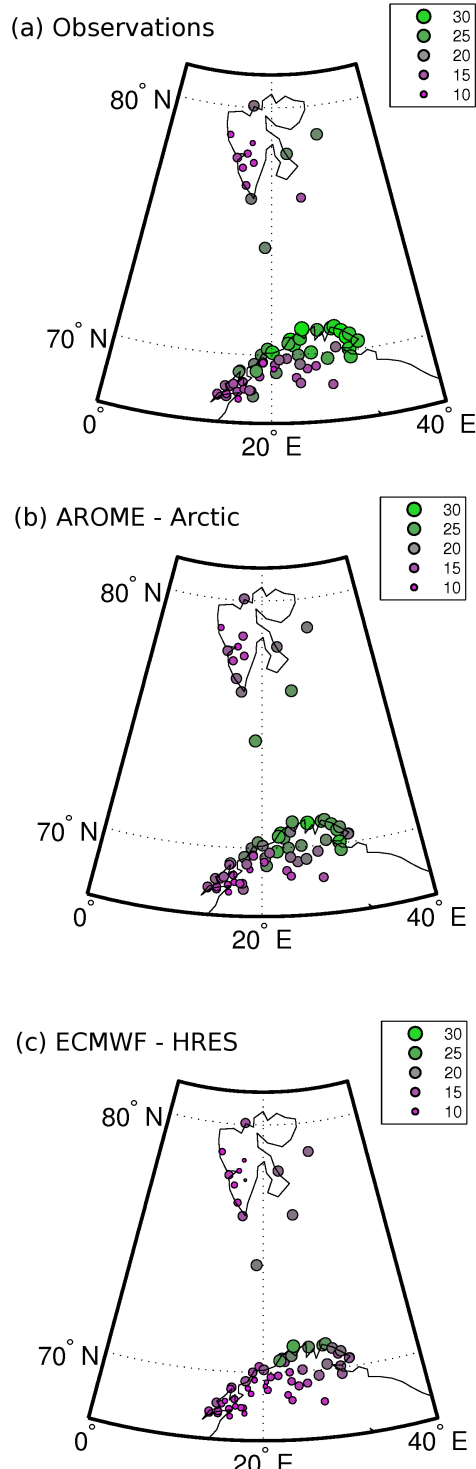


667 FIG. 10. The 95th percentile of U10M wind in (a) AROME Arctic, (b) HRES, (c) ENS, and (d) ERA Interim.

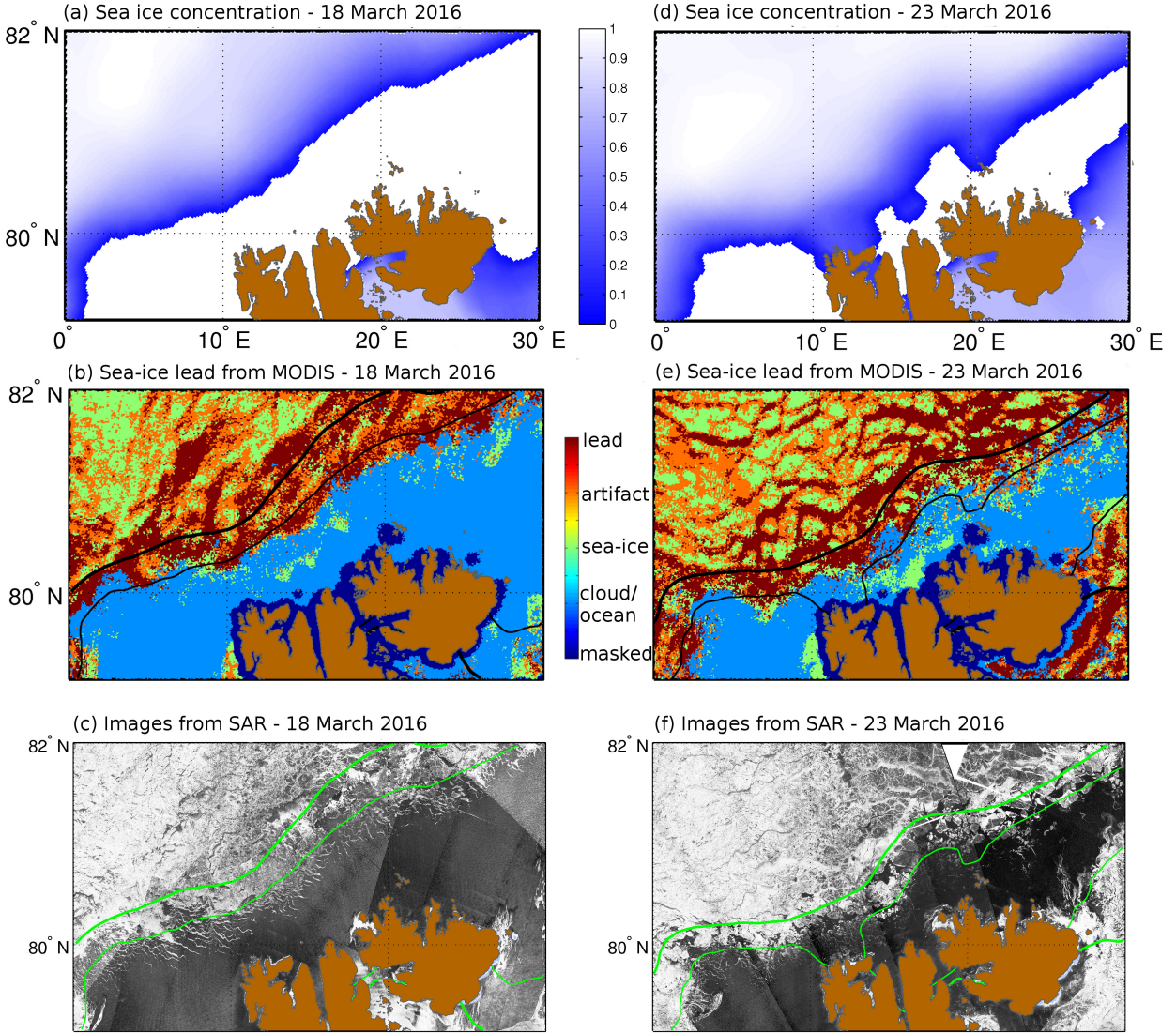
668 The statistics are performed for the time from 1 December 2015 to 30 March 2016.



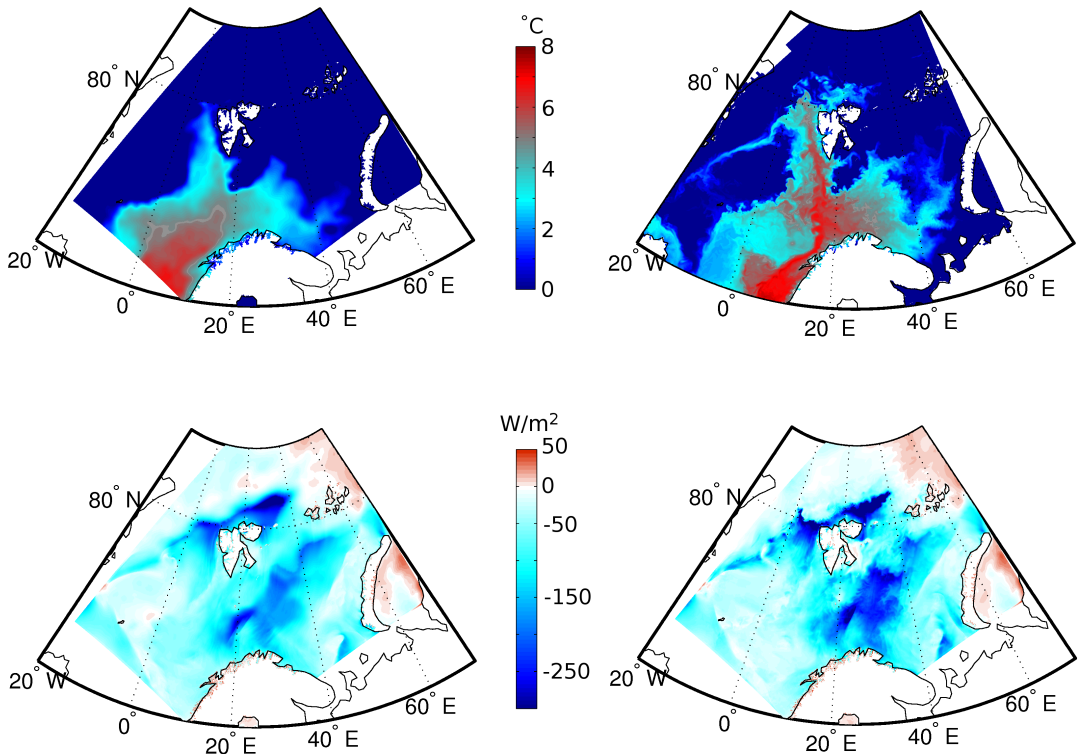
669 FIG. 11. Polar low close to the Norwegian coast at 1800 UTC 8 December 2016. (a) The 10 meter wind speed
 670 of two tracks (approx. 1h apart) from level 2 ASCAT 12.5km resolution product. (b) and (c) the 6 h forecasts
 671 (with analysis time at 1200 UTC 08 December 2016) of 10 meter wind speed from AROME Arctic and HRES,
 672 respectively.



673 FIG. 12. The maximum winds observed within the period from 0000 UTC 08 December 2016 till 0012 UTC
 674 09 December 2016. In (a) from synoptic 10 meter wind observations and in (b) and (c) from forecasts with
 675 analysis time 1200 UTC 07 December 2016 from AROME Arctic and HRES, respectively.



676 FIG. 13. Change of sea-ice concentration and lead structures during a cold air outbreak in March 2016. Left
 677 (right) column of figures shows conditions 18 March 2016 (23 March 2016). In (a) and (d) the OSI-SAF sea-ice
 678 concentration products are shown (it is regridded and postprocessed for the use in AROME). In (b) and (e) a sea-
 679 ice lead product based on MODIS satellite observations is shown (red - lead, orange - artifact, green - sea-ice,
 680 blue - cloud/ocean, dark blue - landmask). For more details see Willmes and Heinemann (2015). Black thick
 681 and thin lines represent 80 and 20 % isolines obtained from OSI-SAF ice concentrations, respectively. In (c) and
 682 (f) a mosaic of SAR images (Surface Backwards Scattering Coefficient of Radar Wave) is shown. Green thick
 683 and thin lines represent 80 and 20 % isolines obtained from OSI-SAF ice concentrations, respectively.



684 FIG. 14. Snapshot (1200 UTC 20 March 2016) of sea surface temperature and turbulent heat flux over the
 685 ocean . The sea surface temperature in (a) of the OSTIA satellite product obtained processed for AROME Arctic
 686 and ECMWF model systems and (b) of the Norwegian METROMS ocean forecasting system (4 km horizontal
 687 resolution). In (c) and (d) the turbulent heat flux in W per m^2 of the operational AROME Arctic system and
 688 from a sensitivity experiment with high-resolution sea surface temperature and sea ice concentration from the
 689 METROMS system.